Chapter 16
Multispectral Face Imaging and Analysis

Andreas Koschan, Yi Yao, Hong Chang, and Mongi Abidi

16.1 Introduction

This chapter addresses the advantages of using multispectral narrow-band images for face recognition, as opposed to conventional broad-band images obtained by color or monochrome cameras (see also the chapter for a discussion of color in face analysis). Narrow-band images are by definition taken over a very small range of wavelengths, while broad-band images average the information obtained over a wide range of wavelengths. There are two primary reasons for employing multispectral imaging for face recognition.

First, we believe that there is distinctive facial information contained in certain narrow spectral bands which can be acknowledged and employed to enhance face recognition performance in comparison to broad-band color or black and white images. Broad-band imaging has the potential to degrade this information that is embedded in the narrow-band image due to the integration process over a wide range of wavelengths during the formation of the image.

Second, multispectral images can separate the illumination information from the reflectance of objects, so that we can use this illumination information to normalize the images. In contrast, it is nearly impossible to separate and employ the illumination distribution information from broad-band images. To verify the effectiveness of

---

A. Koschan (✉) · H. Chang · M. Abidi
Imaging, Robotics, and Intelligent Systems Lab, University of Tennessee, Knoxville, TN 37996, USA
e-mail: akoschan@utk.edu

H. Chang
e-mail: hchang2@utk.edu

M. Abidi
e-mail: abidi@utk.edu

Y. Yao
Visualization and Computer Vision Lab, GE Global Research, Niskayuna, NY 12309, USA
e-mail: yi.yao@ge.com

S.Z. Li, A.K. Jain (eds.), *Handbook of Face Recognition*,
DOI 10.1007/978-0-85729-932-1_16,

multispectral images for improving face recognition, two sequential procedures are taken into account: first, multispectral face image acquisition and second, spectral band selection.

To reduce information redundancy among multispectral images, complexity-guided distance-based band selection is introduced which uses a model selection criterion for an automatic selection. This selection can simplify the imaging process by reducing the number of multispectral images to be taken under a given illumination. In other words, the goal is to identify a small set of optimal multispectral bands to be taken under a given illumination as opposed to acquiring a large set of multispectral bands over the entire visible spectrum.

The performance of selected bands outperforms the conventional images by up to 15%. From the significant performance improvement via complexity-guided distance-based band selection, we conclude that specific facial information carried in certain narrow-band spectral images can enhance face recognition performance compared to broad-band images. In addition, the algorithm is equally useful and successful in a wide variety of recognition schemes.

16.2 Multispectral Imaging

Multispectral imaging is a technique that provides images of a scene at multiple wavelengths and can generate precise optical spectra at every pixel. A *multispectral image* is a collection of several monochrome images of the same scene, each of them taken with additional receptors sensitive to other frequencies of the visible light, or to frequencies beyond visible light, like the infrared region of electromagnetic continuum. Each image is referred to as a *band* or a *channel*. Multispectral imaging produces a three-dimensional image cube with two spatial dimensions (horizontal and vertical) and one spectral dimension. The spectral dimension contains spectral information for each pixel on the multispectral cube. A *multispectral image* can be represented as

$$C(x, y) = \big(\mu_1(x, y), \mu_2(x, y), \ldots, \mu_{N_B}(x, y)\big)^{\mathrm{T}} (\mu_1, \mu_2, \ldots, \mu_{N_B})^{\mathrm{T}}. \tag{16.1}$$

The signal strength $u_k(x, y)$ of a camera sensor in a certain wavelength range, $\lambda_{\min}$ to $\lambda_{\max}$, can be represented as

$$u_k(x, y) = \int_{\lambda_{\min}}^{\lambda_{\max}} R(x, y, \lambda) L(x, y, \lambda) S_k(x, y, \lambda)\, d\lambda, \tag{16.2}$$

with $k = 1, \ldots, N_B$, where $N_B = 1$ for monochromatic images and $N_B = 3$ for three-channel color images. The parameters (x, y) indicate the pixel location in the image. $R(x, y, \lambda)$ is the spectral surface reflectance of the object, $L(x, y, \lambda)$ is the spectral distribution of the illumination, and $S_k(x, y, \lambda)$ is the spectral sensitivity of the camera corresponding to channel k. The entire possible integration wavelength range can be in the visible spectrum, 400–720 nm, or in addition may include infrared spectrum depending on the camera design.

While a monochrome image, $N_B = 1$, has only one band, which is represented as a gray-value image, a multispectral image consists of at least three bands, $N_B \geq 3$. Thus, the image value of a pixel in a multispectral image is represented by vectors with N_B components, as opposed to scalar image values representing pixels in a monochrome image. Although a color image with three bands constitutes in theory the simplest form of a multispectral image, the term is more commonly used for images with more than three bands. One example would be a four-band image using the three *RGB* bands and an additional band beyond the visible spectrum, like in the infrared (IR). Satellites usually take several images from frequency bands in the visible and nonvisible range. No common agreement exists yet on the definition of the term *hyperspectral image*. However, the term is commonly used for images with more than a hundred bands, $N_B > 100$. While *multi* in multispectral means *many* spectral bands, the *hyper* in hyperspectral means *over* as in *more than many* and refers to the large number of measured wavelength bands.

Multispectral imaging can enhance and expand the capability of detecting materials as well as the spatial distributions. For example, spin-offs from NASA's multi- and hyperspectral imaging remote sensing technology, developed for earth resources monitoring, are techniques that combine and integrate spectral with spatial methods. Such techniques are finding use, for example, in medicine, agriculture, manufacturing, and forensics, to mention a few. Multispectral or hyperspectral sensors collect the electromagnetic spectrum at dozens or hundreds of wavelength ranges in the visible and near infrared spectra. Spectral resolution of a multispectral sensor is higher and is defined as a measure of the narrowest spectral wavelength that can be resolved by a sensor. Due to hardware limitations (most of the color cameras are RGB cameras) all the spectral information is converted to RGB triplets during image acquisition. It is a projection from an infinite-dimensional color space to a three-dimensional space, or many-to-one projection, which results in colors with different spectral distributions giving the same RGB response. Colors with the same tristimulus data but with different power distributions are called metameric colors.

The compromise between tristimulus data collection and spectrographic information is the employment of multiple (more than three) color filters with narrow bandwidth mounted either between the lens and the sensor of the camera or in front of the camera lens. The most common procedure is to place the filters in front of the camera lens. Such an apparatus allows to obtain spatial information about the imaged scene at high spectral resolution. The collection and processing of 2D images of the same scene under many spectral (often narrow band-pass) filters, particularly in the visible range, is often referred to as multispectral imaging.

16.2.1 Multispectral Imaging Using Rotating Wheels

In recent years, modern spectral image capture systems tend to rely on combinations of CCD cameras with various types of narrow or broad band filters. The images are then processed using common high-capacity computers with software developed to

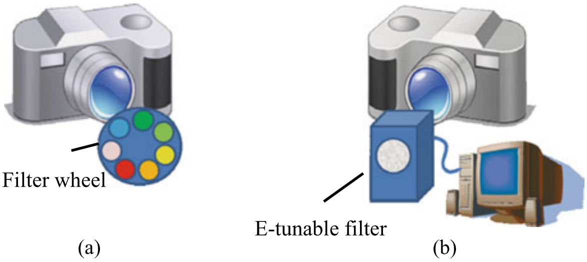

Fig. 16.1 Multispectral imaging systems. **a** Camera with rotating wheel and **b** camera with electronically tunable filter in front of lens

properly treat the spectral data. Therefore, capturing multispectral images can be accomplished by swapping narrow band-pass glass filters in front of the camera lens. It is common for such filters to be mounted in a filter wheel. Nowadays, color filters with minimum bandwidth of approximately 10 nm are available off-the-shelf. Different filters and combinations were proposed for different applications. Figure 16.1 illustrates the principle of mounting a filter wheel in front of the camera lens.

Ohta et al. [33] used a film-based system for multispectral image capture. Their system used a mechanical rotating filter wheel with eight gelatin filters to image rigid objects. Only rays within a small wavelength band experience constructive interference and pass through the interference filters. In such use, interference filters offer a large aperture, large field of view, and good optical quality. Tominaga proposed a camera system with six color filters [45], which had six spectral channels of the color filters' fixed wavelength bands.

Fixed-filter systems have intrinsic restrictions: (1) the selection of color filters and the number of filters are limited; (2) filters with a narrow band-pass are difficult to build; (3) moving parts are necessary to select the filters since it is a mechanical system. Due to the latter restriction, time on the order of seconds can be required to step filters in a preset sequence and vibrations of the imaging system may occur. These systems are commonly employed for multispectral imaging of rigid objects where image acquisition time can be long.

16.2.2 Multispectral Imaging Using Electronically Tunable Filters

A faster and more flexible way of multispectral imaging involves electronically tunable filters (ETFs). A tunable filter is a device whose spectral transmission can be electronically controlled through the application of voltage or acoustic signals. In addition, the large aperture and imaging capability of these devices represent a distinct advantage over conventional dispersive spectral analysis techniques. Unlike conventional filter wheels, there are no moving parts and no discontinuity in the spectral transmission range, thus providing finer spectral sampling, and rapid and random switching between color bands. Also, ETFs are light weight, making them attractive for airborne or remote sensor platforms.

Electronically tunable filters offer the fastest, most accurate and flexible color filtering techniques that are currently available. The majority of ETFs can be classified under three operational categories: (1) Acousto-Optical Filters based on diffraction, (2) Fabry–Perot Filters based on optical interference, and (3) Liquid Crystal Filters based on birefringence. Although each of the three types of ETFs is based on different principles of optics, each of them is successful in selecting individual band pass over a continuum of spectral ranges with high speed and accuracy. Figure 16.1 shows two different designs of multispectral imaging systems: (a) a camera with a rotating wheel and (b) a camera with an electronically tunable filter in front of the lens.

The operation of the *Acousto-Optic tunable filter (AOTF)* is based on the interaction of electromagnetic and acoustic waves. The main module of an AOTF is an optically transparent crystal that possesses a certain combination of optical and acoustic properties. While the incoming light falls on the crystal, a radio-frequency acoustic wave is sent to the crystal simultaneously. It is used in creating a refractive index wave within the crystal. The incident beam when passing through the refractive index wave breaks into its component wavelengths. In the end, a single wavelength of light is selected for transmission. Proper design makes one of these wavelengths much more prominent and that becomes the output color of the filter. The wavelength of the filtered light is selected by changing the frequency of the acoustic wave. AOTFs are lightweight and very fast spectral filtering devices. One disadvantage of such devices is the requirement that the incident light be collimated [16].

Another category of electronically tunable filters applies the principle of *optic interference*. A Fabry–Perot cavity is the basic component consisting of two parallel planar surfaces, whose inner face is coated with partially transparent films of high reflectivity, enclosing a rectangular volume of air or some dielectric material. Light enters through one of the partially transparent mirrors and is multiply reflected within the cavity. The multiply transmitted rays interact with each other, creating optical interference effects, which result in the transmission, through the opposite semitransparent mirror, of only one particular wavelength and its harmonics. To block the unwanted harmonics, often two cavities in a row are employed, constituting a *dual tunable Fabry–Perot (DTFP)* device [39]. *Electro-optic Fabry–Perot (EOFP)* devices adjust the bandpass spectrum by varying the refractive index of the cavity through the application of electric potential. Recently, *liquid crystals (LCFP)* are employed as cavity medium. On average, single-cavity ETFs can select the output wavelength out of an input range that is no larger than 100 nm wide. Thus, a cascade of Fabry–Perot cavities is needed in order to have an EOFP that can analyze the entire visible spectrum. Such designs are more costly and have a lower transmission rate (20–50% instead of 90% for a single cavity [39]).

Recently, the Applied Spectral Imaging SpectraCube has been introduced, which is an interferometry-based portable digital camera. This camera is based on the idea that if interference of the color signal is created and measured, the spectrum of the original signal can be recovered applying the *inverse Fourier transform*. With this device, a full 2D array of spectra is captured at once and, unlike filter-based systems, a single exposure is acquired. The spectral resolution of this device can be set higher than most filter-based systems (e.g., about 4 nm), but it also comes

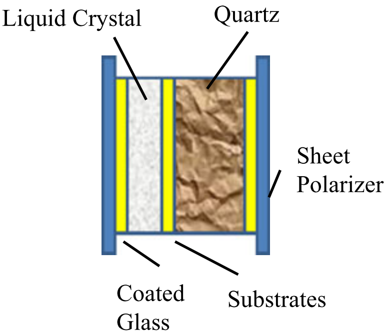

Fig. 16.2 Principle design of a Liquid Crystal Tunable Filter element (after [14])

at a high expense. Moreover, the single-image acquisition time ranges from 30 to 150 seconds (depending on spatial and spectral resolution and aperture) [13].

The third and most commonly used category of filter devices is *liquid crystal tunable filters (LCTFs)*, which use electrically controlled liquid crystal elements to select a specific visible wavelength of light for transmission through the filter at the rejection of all others. A typical LCTF is built using a stack of polarizers and tunable retardation (birefringent) liquid crystal plates (cp. Fig. 16.2). The LCTF is polarization sensitive. Switching speed is limited by relaxation time of the crystal and is of the order of ~50 ms. Special devices can be designed for fast switching (~5 ms) through a short sequence of wavelengths. Spectral resolution, or band pass, of the LCTF is typically of the order of several nm, although a narrower band pass can also be constructed [14].

For a multispectral imaging system employing a LCTF, the camera response u_{λ_k} corresponding to band k centered at wavelength λ_k within the range, $\lambda_{k,\min}$ to $\lambda_{k,\max}$, can be represented as (compare (16.2))

$$u_{\lambda_k} = \int_{\lambda_{k,\min}}^{\lambda_{k,\max}} R_{\lambda_k}(\lambda) L_{\lambda_k}(\lambda) S_{\lambda_k}(\lambda) T_{\lambda_k}(\lambda)\, d\lambda \tag{16.3}$$

for $k = 1, 2, \ldots, N_B$ where k indicates the kth spectral band, N_B is the total number of bands, and T_{λ_k} is the spectral transmittance of the LCTF. (x, y) is omitted for simplicity. R_{λ_k} is the spectral surface reflectance of the object (here the face), L_{λ_k} is the spectral distribution of the illumination, and S_{λ_k} is the spectral sensitivity of the camera corresponding to band k. the imaging process is illustrated in Fig. 16.3.

Nowadays, a considerable variety of Liquid Crystal Tunable Filters, Acousto-Optic Tunable Filters, and Electro-Optic Fabry–Perot is available in the market. Most of them have comparable performance characteristics. Table 16.1 lists typical characteristics of ETFs (after [39]).

Spectroradiometers are a precise alternative to filter-based systems. After light passes through the shutter, it is directed to a concave diffraction grating that breaks up the signal into a photosensitive array and focuses the diffracted signal onto a photosensitive array. These devices have a very high spectral resolution, precision, and stability [13]. Nevertheless, one disadvantage of spectroradiometers is that they

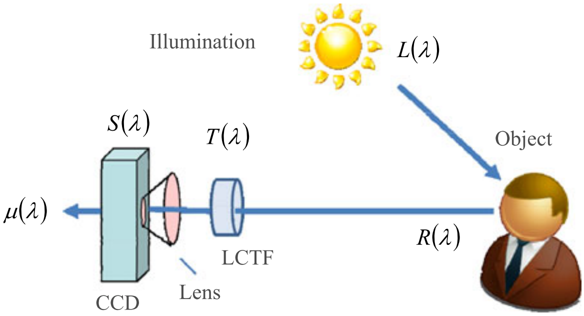

Fig. 16.3 The camera response is the result of integration of all the factors involved, including the spectral distribution of illumination, reflectance of the object, the transmittance of the filter, and the spectral response of the camera

Table 16.1 Typical tunable filter characteristics (after [39])

Attributes	AOTF	EOFP	LCTF
Operating spectral range	200–5000 nm	400–1550 nm	400–1800 nm
Max width of tunable range	700 nm (vis + NIR) 3900 nm (MIR)	100 nm	450 nm (vis + NIR) 950 nm (MIR)
Min. output bandwidth	0.4 nm	0.05 nm	5 nm
Max. output bandwidth	50 nm	30 nm	10 nm
Mean error in central wavelength	1 nm (varies with l)	1 nm (varies with l)	0.5 nm
Average transmission rate	98%	20–50%	20–50%
Transmission rate over wavelength	constant	increases with wavelength	increases with wavelength
Out of band transmission	0.05–0.1%	0.5–1%	0.01–0.05%
Tunability time	~15–30 ms	~40 ms (LCFP) ~4 ms (DTFP)	~50 ms
Incident light limitations	requires collimated light	none	none

measure only single points. Therefore, it is nearly impossible to use them to capture a full scene.

Multispectral imaging systems with electronically tunable filters have been used by several research groups [17, 20, 21, 34, 35, 40, 45]. The Munsell Color Science Laboratory initiated efforts with multispectral images using a LCTF over the visible spectrum, especially for high resolution art portrait reconstruction [20, 21]. They also acquired the Lippmann2000 database [40] that contains spectral images of several objects including faces from 4 Caucasians and 3 East-Asians. This data was acquired by a film camera with approximately 15 to 25 second lapses between exposures and 16 exposures for each person, under flash lighting.

Pan et al. [34, 35] acquired spectral images over the near infrared spectrum (700–1000 nm) and demonstrated that spectral images of faces acquired in the near infrared range can be used to recognize individuals. Until now, not much research has been done using multispectral imaging in the visible domain to address the problem of face recognition, especially with respect to changes in illumination conditions.

The multispectral databases mentioned above either have very few data records or are not in the visible spectrum. In addition, these datasets were not compared with conventional face images by recognition engines.

16.2.3 Multispectral Band Selection

When a large amount of multispectral data has to be analyzed, it is very desirable to reduce the initial information without losing classification accuracy to a significant degree. This reduction can be achieved by two methodologies: feature extraction [4, 11, 12, 18, 23, 24, 29–31, 36, 41, 42, 44] or band selection [6, 26–28, 38, 43, 46].

In feature extraction, a new and reduced data set representing the transformed initial information is obtained, whereas in band selection a subset of relevant data from the original bands is chosen. Compared to feature extraction, band-selection methods identify a subset of the original spectral bands that contains most of the characteristics. Selecting a subset of relevant bands from the original set allows the process of image acquisition to be reduced to a certain number of bands instead of dealing with the entire set of data and, therefore, simplifying image acquisition and analysis.

Feature extraction transfers the data into a lower dimensional space. Features are extracted from the original spectral bands to construct a lower-dimension feature space. Thereby the original data are transformed into the destination feature space through projections such as Projection Pursuit (PP) [31], Principal Component Analysis (PCA) [12], locally linear embedding [41], Isomap [44] and subspace theory [18, 36, 42], wavelet transform [4, 23], and Independent Component Analysis (ICA) [11, 30]. These projections preserve most desired information but change the physical meaning of each spectral band. These methods rank the influence of each single spectral band on the new lower dimensional space. Bands with the highest influence are considered to include more information and are therefore selected [1, 7]. It is nearly impossible to predict the best dimension required for dimension reduction without significant loss of information. In addition, the data is transformed and no longer exists as original data. Some crucial and critical information may have been compromised and distorted.

The goal of band selection is to minimize information loss from the information preservation point of view. Mutual information is a good candidate for band selection as a measure of independence between random variables. For example, Sotoca et al. [43] used conditional entropy as an approximation of mutual information to measure the independent information carried by one band given a sub-band set. Peng et al. [38] argued that maximizing the relevance between each individual band and the class is equivalent to the maximum dependency criterion if one band is selected at a time. Their method needs samples from inside the class, as well as outside of the class, to evaluate the relevance of each individual band with the class. Thus, it is not applicable if no samples outside the class are available. Basically, the method employs an unsupervised band selection criterion to obtain the relevant spectral bands from a set of sample images, while minimizing the dependent information between spectral bands and maximizing the conditional entropies of the selected bands [43].

In general, the problem of subset selection using numerical techniques for model selection requires two components: a search algorithm and an evaluation criterion.

First, an algorithm is needed for the efficient search of the solution space, such as greedy and genetic algorithms. Exhaustive search [25] over the entire feature data set and the branch-and-bound algorithm [5] has rarely been used in the analysis of high-dimension data due to the computational costs even though they lead to an optimal solution. Heuristic search methods such as hill climbing, backward elimination, forward selection, and stepwise selection are commonly used.

Second, a criterion or measure is needed for the comparison and evaluation of competing models to guide the search. The criterion can be based on human perception, which makes it hardware dependent, participant dependent, quite subjective, and also time consuming. Other criteria mentioned in the literature include first or second spectral derivatives [1]. Entropy is interpreted as a measure of stability of each individual wavelength band. Low entropy values correspond to low uncertainties and thus bands with small entropy are considered good feature bands. Bassett and Shen [2] used entropy to measure the difference between different classes.

Commonly, researchers apply band selection with the consideration of classification outputs. In [1], the issue of hyperspectral bands and method selection using unsupervised and supervised methods driven by classification accuracy and computational cost is addressed. Their formulation is more general by optimizing over several methods and the combinations of supervised and unsupervised methods evaluations. One goal of band selection is to identify a reflectance feature that remains invariant when the viewing conditions change. Wang and Angelopoulou [47] propose a technique for extracting color information that is invariant to geometry and incident illumination. They examine the rate of change in reflected intensity with respect to wavelength over the visible part of the electromagnetic spectrum. For diffuse surfaces the only factor that contributes to variations over the wavelength is the albedo of the surface independent of the particular model of reflectance.

16.3 The IRIS-M^3 Face Database

A multispectral and multi-illuminant face database was acquired at the IRIS Lab to support research in multispectral image analysis for face recognition. The database includes indoor and outdoor images taken under controlled and uncontrolled illumination situations. During image acquisition a liquid crystal tunable filter in the visible spectrum was used, which provided narrow band filters at different wavelengths between 400 nm and 720 nm. The multispectral face database has noteworthy characteristics. It is the first database with registered images in the visible, multispectral and thermal modalities, coupled with spectral distributions of the illumination sources used during acquisition. Participants were imaged under various illumination conditions such as halogen light, fluorescent light and day light. Another interesting feature is the large number of multispectral bands available in the database with 25 bands per participant and a total of 82 participants.

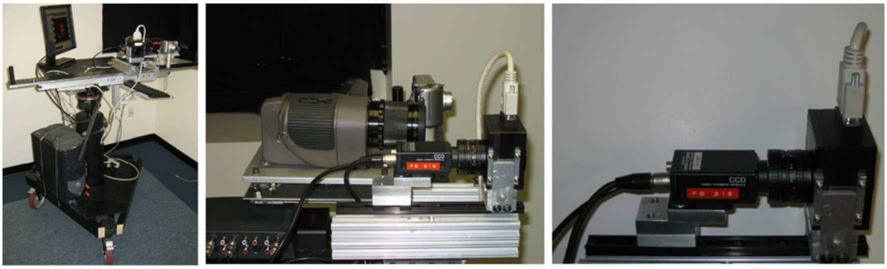

(a) (b) (c)

Fig. 16.4 **a** The all-inclusive multimodal and multispectral mobile imaging system, **b** lateral view of the multimodal imaging system, and **c** the multispectral imaging components (from [10])

Fig. 16.5 Narrow-band transmittances of the LCTF from 400 nm to 720 nm with 10 nm increments

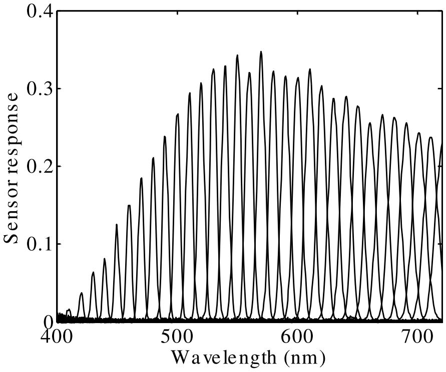

The multispectral imaging system shown in Fig. 16.4 is integrated on a translational platform to acquire well-aligned face images in a short period of time. This allows the participants to maintain their expression and pose. The mobile imaging system shown in Fig. 16.4(a) consists of a multispectral imaging module, a digital RGB camera, a near infrared camera, a spectrometer, a frame grabber and an onboard computer. Figure 16.4(b) shows the lateral view of the multimodal imaging system. The multispectral imaging components shown in Fig. 16.4(c), consist of a Sony XC-75 monochrome camera and a VariSpec liquid crystal tunable filter, which can electronically tune a narrow band filter centered at various wavelengths in visible spectrum. The LCTF provides narrowband filters with a full width-at-half-maximum bandwidth of 7 nm. A maximum of 331 narrow-band multispectral images can be acquired by continuously tuning the LCTF. The aperture of the LCTF is 35 mm and the field of view is ±7°. A wide angle lens is mounted on the monochrome camera (Sony XC-75) and this is coupled with the LCTF through a hardware interconnection. The camera auto-gain is set to 0 dB in order to acquire raw data. The black current of the Sony XC-75 is measured by covering the lens and reading the pixel values of black images. After averaging, the typical black current is 4 to 5 values out of 256. The transmittance of the used LCTF is different at different wavelengths as shown in Fig. 16.5.

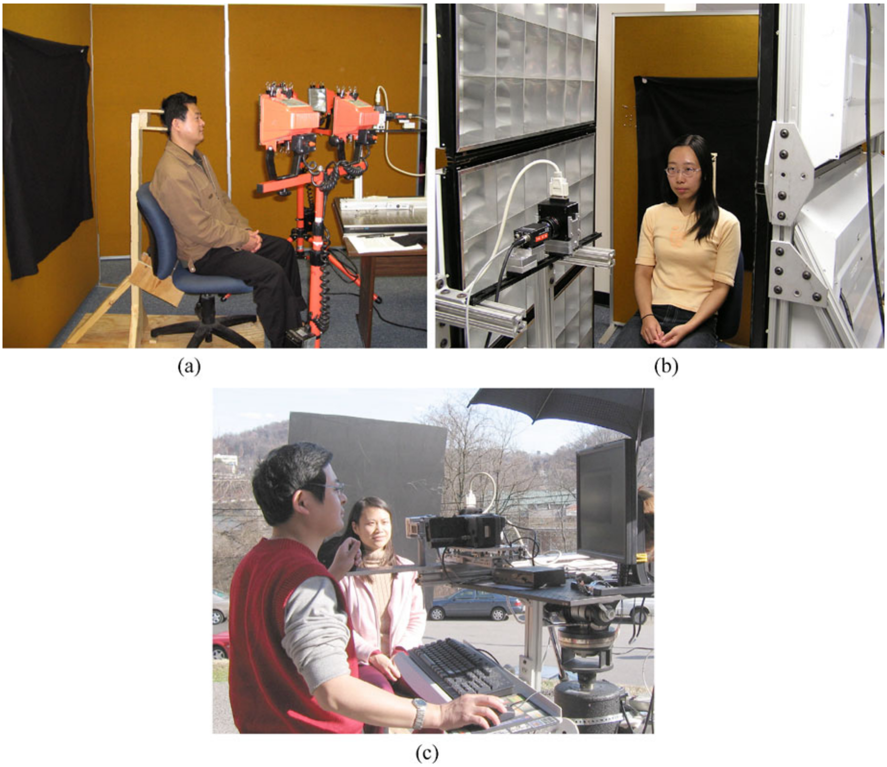

Fig. 16.6 Three illumination setups, **a** quadruple halogen lights with a pair on each side, **b** a pair of fluorescent light panels, and **c** daylight with side illumination (from [10])

Three datasets were acquired with three different illumination scenarios: halogen light, fluorescent light and daylight. The three illumination setups are shown in Fig. 16.6. The quadruple halogen lights with a pair on each side of the participant are shown in Fig. 16.6(a). The second illumination setup was a pair of fluorescent light panels (fluorescent-1) shown in Fig. 16.6(b). We assume that the indoor illuminations, halogen light and fluorescent light, are homogeneously distributed on the face and have stable spectral power when they are lit. The daylight face data was acquired with side illumination due to the fact that many participants were unable to maintain pose or expression with bright sun light shining directly into their eyes. We grouped the outdoor data acquisition into 8 different sessions according to weather conditions and acquisition time. The weather conditions ranged from sunny to cloudy and the passing clouds caused rapid changes in lighting conditions. An outdoor data acquisition setup with side illumination is shown in Fig. 16.6(c). For comparison an additional set of images was acquired with a Canon A80 under another type of fluorescent light (fluorescent-2). The illuminations are characterized during the database collection via the use of a light meter and a spectrometer. An

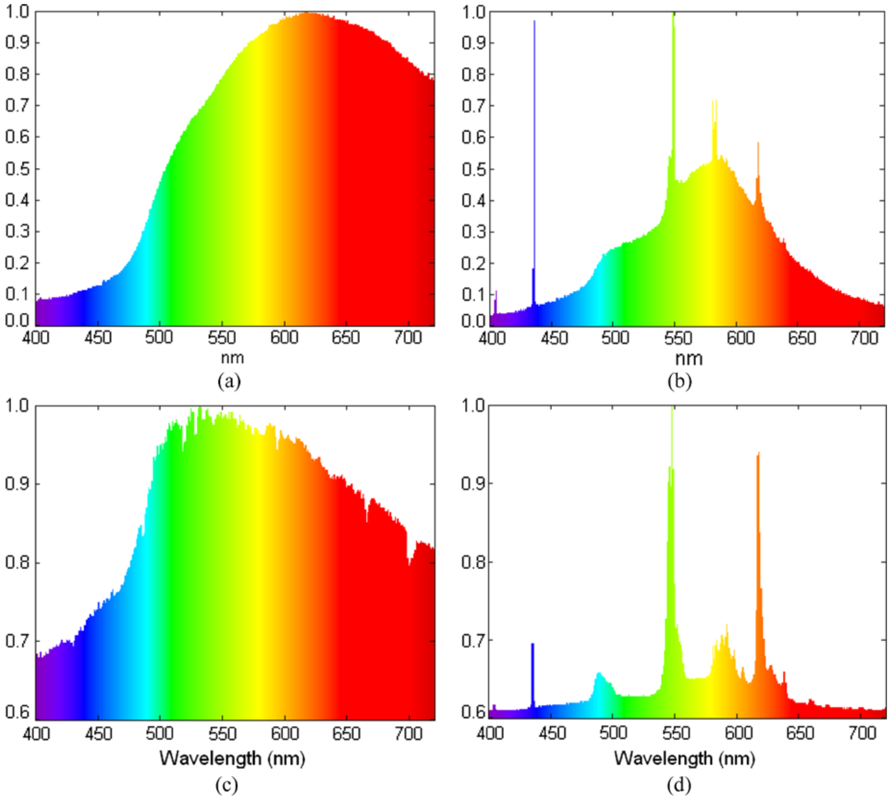

Fig. 16.7 Normalized spectral power distribution of **a** halogen light **b** fluorescent light, **c** day light, and **d** another fluorescent light (from [10])

EasyView30 light meter was used to measure the illuminance and an Ocean Optics USB2000 Spectrometer was used to measure the irradiance of the illuminant.

The spectral power distributions (SPDs) of four different illuminants used during the data acquisition process are shown in Fig. 16.7. The SPD of halogen light (a) is very smooth and the peak is at the orange part of the spectrum. The SPD of the fluorescent light panel (b) is spiky at certain wavelengths. The day light depicted in Fig. 16.7(c) tends to have more green and blue components in comparison to the other two illuminants. A second fluorescent light was used during the image acquisition process which has a different SPD than the first fluorescent light (see Fig. 16.7(d)).

There are a total of 82 participants of different ethnic groups, ages, facial hair characteristics, and genders in the database with 2624 face images. The corresponding illumination information for each image is recorded using the spectrometer. The image resolution is 640 by 480 pixels and the eye-to-eye distance is about 120 pixels. The database was collected in 11 sessions between August 2005 and May 2006 with some participants being photographed multiple times. Figure 16.8 shows sam-

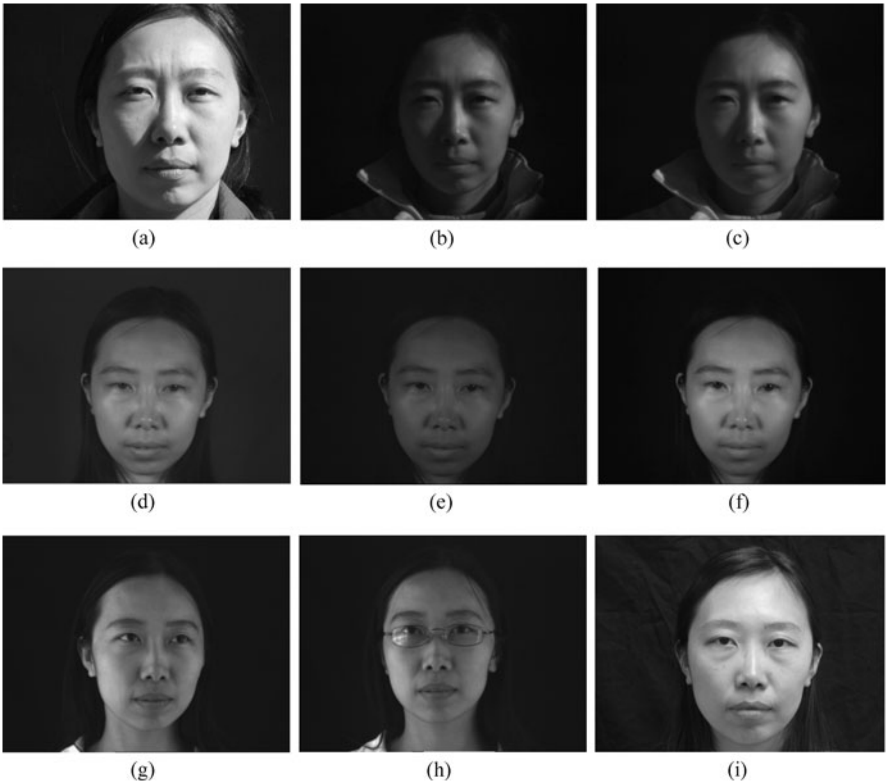
(a) (b) (c) (d) (e) (f) (g) (h) (i)

Fig. 16.8 Sample images in a data record in the IRIS-M^3 database; **a** side illumination under daylight, **b** band 640 nm multispectral image under daylight, **c** band 720 nm spectral image under daylight, **d** under indoor halogen light, **e** band 640 nm spectral image under indoor halogen light, **f** band 720 nm spectral image under indoor halogen light, **g** under fluorescent with slightly facing her left, **h** under fluorescent with glasses, and **i** under another fluorescent light (from [10])

ples from one data record in the IRIS-M^3 database with variations in lighting conditions and elapsed time. The database contains 76% males and 24% females; the ethnic diversity was defined as a collection of 57% Caucasian, 23% Asian (Chinese, Japanese, Korean and similar ethnicity), 12% Asian Indian, and 8% of African Descent. Figure 16.9 illustrates by example the demographics of the database including different ethnicities, age groups, facial hair characteristics, and genders.

16.4 Complexity-Guided Distance-Based Band Selection

In this section, a complexity-guided distance-based band selection method is introduced as a key step in multispectral image processing aimed at improved face recognition. Let the total number of multispectral bands be N_B and λ_k denotes the central wavelength of the kth band. The complete set of multispectral bands

Fig. 16.9 Examples of 6 subjects, **a** male Asian under fluorescent light, **b** female Caucasian under fluorescent light, **c** male Caucasian under fluorescent light, **d** female of African Descent under fluorescent light, **e** male Asian Indian under daylight, **f** female Asian under daylight, **g** male Caucasian under daylight and **h** female of African Descent under daylight (from [10])

is $\mathscr{B} = \{\lambda_k \mid k = 1, \ldots, N_B\}$. The proposed method automatically searches for an optimal subset $\mathscr{B}_{\text{opt}} \subseteq \mathscr{B}$ such that the fused images from $\mathscr{B}_{\text{opt}}$ can outperform conventional broad-band images. To achieve such a goal, the proposed method explores a divergence based distance measure and defines a new redundancy measure to quantitatively describe the correlation among multiple spectral bands. The probabilistic distance measure insures that the selected subset is sufficient for improving recognition rate whereas the redundancy measure insures that the subset is necessary with a minimum number of selected bands.

First, let us define the genuine and imposter sets of each spectral band. In multispectral face recognition, a gallery consists of a set of samples $\{g_1, \ldots, g_N\}$, where N is the total number of subjects in the gallery. When a probe image p_j^k collected at the kth spectral band is presented to a system, it is compared with all the samples in the gallery. The comparison between a probe p_j^k and each gallery sample g_i produces a similarity score S_{ij}^k. These similarity scores can be divided into two groups for each spectral band, referred to as the genuine $\mathscr{G}_k$ and imposter $\mathscr{I}_k$ sets. The genuine and imposter sets are defined as: $\mathscr{G}_k = \{S_{ij}^k \mid i = j\}$ and $\mathscr{I}_k = \{S_{ij}^k \mid i \neq j\}$, respectively. In other words, the genuine set contains the similarity scores with probe and gallery images from the same subject whereas the imposter set consists of similarity scores with the probe and gallery images from different subjects.

Given the genuine and imposter sets of the multiple spectral bands, we first estimate the distributions or equivalently the probability density functions (PDFs) of their respective similarity scores, $\hat{p}_{G,k}(x)$ and $\hat{p}_{I,k}(x)$, and then compute the distance between these two PDFs producing a distance measure Q_k for each spectral band. In the algorithm proposed in [8, 9], the N_{opt} spectral bands with the highest Q_k values are selected. Two drawbacks are observed. Firstly, the number of bands N_{opt} is user specified, which cannot be optimized automatically. Secondly, bands with the highest N_{opt} distance measures are selected disregarding the latent redundancy among these bands. In this chapter, we investigate appropriate approaches to select a subset with minimum redundancy and to automatically determine the optimal number of sub-bands.

In [8, 9], it has been demonstrated that an important criterion of selecting the appropriate spectral bands is the separation between the similarity scores of the genuine and imposter set. Therefore, we obtain a set of ordered sub-bands according to the distance measure: $\mathscr{B} = \{\lambda_{k_i} \mid i = 1, \ldots, N_B\}$ with $Q_{k_i} \geq Q_{k_{i+1}}$, which means that the first and last sub-bands in $\mathscr{B}$ have the highest and lowest distance measures, respectively. We start with the spectral band that yields the highest distance measure λ_{k_1}: $\mathscr{B}_1 = \{\lambda_{k_1}\}$. The questions are how to select the next band that brings in the most information and when to stop the selection process. These two questions correspond to the problems of selecting the optimal subset and deriving the optimal number of sub-bands. To answer these two questions, we define a quantitative measure that describes the redundancy among bands.

At the mth iteration and given the current selected subset $\mathscr{B}_m$, we obtain the set of candidate sub-bands: $\overline{\mathscr{B}} = \mathscr{B} - \mathscr{B}_m$. According to the order of the sub-bands in $\overline{\mathscr{B}}$, we add one sub-band λ_{k_i} into $\mathscr{B}_m$: $\mathscr{B}_{m,k_i} = \mathscr{B}_m \cup \{\lambda_{k_i}\}$ and evaluate the redundancy measure of the augmented set: $R(\mathscr{B}_{m,k_i})$. We increase i if the redundancy measure decreases and stop if the redundancy measure begins to increase or all the candidate sub-bands in $\overline{\mathscr{B}}$ have been examined. If $R(\mathscr{B}_{m,k_i}) < R(\mathscr{B}_m)$, the newly elected band λ_{k_i} is added to $\mathscr{B}_m$ forming a new band set $\mathscr{B}_{m+1} = \mathscr{B}_{m,k_i}$ and the process iterates. Otherwise, output the current $\mathscr{B}_{\text{opt}} = \mathscr{B}_m$ as the optimal subset. Algorithm 16.1 describes the detailed steps of the proposed band selection algorithm.

In the election process at each iteration, we start from the sub-band with the highest distance measure in the candidate set and search for the appropriate sub-band according to the descending order of the distance measure. The search is stopped once the redundancy measure of the augmented set begins to increase. In so doing, we are able to locate the sub-band that produces a relatively high distance measure and a relatively low redundancy measure simultaneously.

In the following sections, we will describe the major steps in the proposed algorithm, namely PDF estimation, distance measure computation, and the definition of the redundancy measure.

Algorithm 16.1: Multispectral band selection

```
Input: $\mathscr{G}_k$, $\mathscr{I}_k$
    Compute PDFs of the genuine and imposter sets, $\hat{p}_{G,k}(x)$ and $\hat{p}_{I,k}(x)$
    Compute the probabilistic distance measure $Q_k$ between $\hat{p}_{G,k}(x)$ and $\hat{p}_{I,k}(x)$
    Obtain $\mathscr{B} = \{\lambda_{k_i} \mid i = 1, \ldots, N_B\}$ with $Q_{k_i} \geq Q_{k_{i+1}}$
    Initialize $R(\Phi) = \infty$, $\mathscr{B}_o = \Phi$, $\mathscr{B}_1 = \{\lambda_{k_1}\}$, and $m = 1$
    while $R(\mathscr{B}_m) < R(\mathscr{B}_{m-1})$ do
        Initialize $i = 2$
        Obtain $\overline{\mathscr{B}} = \mathscr{B} - \mathscr{B}_m$
        Obtain $\mathscr{B}_{m,k_1} = \mathscr{B}_m \cup \{\lambda_{k_1}\}$ and $\mathscr{B}_{m,k_2} = \mathscr{B}_m \cup \{\lambda_{k_2}\}$ with $\lambda_{k_1}, \lambda_{k_2} \in \overline{\mathscr{B}}$
        Compute $R(\mathscr{B}_{m,k_1})$ and $R(\mathscr{B}_{m,k_2})$
        while $R(\mathscr{B}_{m,k_i}) < R(\mathscr{B}_{m,k_{i-1}})$ do
            Obtain $\mathscr{B}_{m,k_{i+1}} = \mathscr{B}_m \cup \{\lambda_{k_{i+1}}\}$ with $\lambda_{k_{i+1}} \in \overline{\mathscr{B}}$
            Compute $R(\mathscr{B}_{m,k_{i+1}})$
            Increase $i$ by one
        end while
        Add $\lambda_{k_{i-1}}$ to $\mathscr{B}_m$: $\mathscr{B}_{m+1} = \mathscr{B}_m \cup \{\lambda_{k_{i-1}}\}$
        Increase $m$ by one
    end while
Output: $\mathscr{B}_{\text{opt}} = \mathscr{B}_{m-1}$
```

16.4.1 Kernel Density Estimation

Kernel density estimation (KDE) is used to obtain the probability density function because the underlying density can be estimated without assuming a particular form or structure [37]. Formally, kernel estimators smooth out the contribution of each observed data point over a local neighborhood of that data point. Letting $K()$ denote the Kernel function and h its smoothing parameter/bandwidth, the estimated density at any point x is given by [48]:

$$\hat{p}(x) = \frac{1}{Nh} \sum_{i=1}^{N} K\left(\frac{x - x_i}{h}\right). \tag{16.4}$$

Recall that N is the total number of subjects in the gallery and that S_{ij}^k denotes the similarity score between the gallery sample of the ith subject and the probe of the jth subject collected from the kth spectral band. From the similarity scores of various subjects, the distributions of the genuine and imposter sets, $\hat{p}_{G,k}(x)$ and $\hat{p}_{I,k}(x)$, are estimated using KDE:

$$\hat{p}_{G,k}(x) = \frac{1}{Nh_{G,k}} \sum_{i=1}^{N} K\left(\frac{x - S_{ii}^k}{h_{G,k}}\right), \tag{16.5}$$

$$\hat{p}_{I,k}(x) = \frac{1}{N(N-1)h_{I,k}} \sum_{i=1}^{N} \sum_{j=1, j\neq i}^{N} K\left(\frac{x - S_{ij}^k}{h_{I,k}}\right). \tag{16.6}$$

The bandwidth parameter controls the smoothness of the density estimation and determines the trade-off between the bias and variance. Often h is chosen as to minimize the Asymptotic Mean Integrated Square Error (AMISE) [32]:

$$h_{\text{AMISE}} = \left[\frac{\rho(K)}{N\mu(K)^2\sigma(p')}\right]^{1/3} \tag{16.7}$$

where $\rho(K) = 2\int_{-\infty}^{\infty} xK(x)K_I(x)\,dx$, $\mu(K) = \int_{-\infty}^{\infty} x^2K(x)\,dx$, and $\sigma(p') = \int_{-\infty}^{\infty} p'(x)^2\,dx$ with $K_I(x) = \int_{-\infty}^{x} K(x)\,dx$.

16.4.2 Probabilistic Distance Measure

Probabilistic distance measures are used here to measure the similarity between the genuine and imposter sets. Probabilistic distance measures have been used in many research areas such as probability and statistics, pattern recognition, information theory, communication, and so on. Here, the symmetric Kullback–Leibler divergence, referred to as the Jeffrey divergence, [22], is used:

$$Q_k = \int \left[\hat{p}_{G,k}(x) - \hat{p}_{I,k}(x)\right] \log \frac{\hat{p}_{G,k}(x)}{\hat{p}_{I,k}(x)}\,dx. \tag{16.8}$$

16.4.3 Redundancy Measure

The redundancy measure is derived in the framework of multivariate model selection with penalty on correlation between sub-bands. The core process is a multivariate kernel estimation on the similarity scores of the genuine sets and the evaluation of redundancy based on information complexity.

In the previous section, the PDFs, $\hat{p}_{G,k}(x)$ and $\hat{p}_{I,k}(x)$, of the kth sub-band are estimated independently of other sub-bands. To incorporate the correlation between sub-bands, we employ multivariate KDE. Given the set $\mathscr{B}_m$, the dimension of the multivariate KDE is the number of sub-bands under consideration, $N_k = |\mathscr{B}_m|$. Let $\mathbf{s}$ denote the multivariate vector and $\mathbf{s}_i$ represent the ith data point where $\mathbf{s}_i = [S_{ii}^k]$ with $\lambda_k \in \mathscr{B}_m$. The multivariate KDE is given by:

$$\hat{p}(\mathbf{x}) = \frac{1}{N(2\pi)^{N_k/2}} |H|^{-1/2} \sum_{i=1}^{N} K\left[(\mathbf{x} - \mathbf{s}_i)H^{-1}(\mathbf{x} - \mathbf{s}_i)\right]. \tag{16.9}$$

If the sub-bands in $\mathscr{B}_m$ are independent, the multivariate KDE reduces to:

$$\hat{p}(\mathbf{x}) = \frac{1}{N}\sum_{i=1}^{N}\left[\prod_{k=1}^{N_k}\frac{1}{h_k}K\left(\frac{x_k - S_{ii}^{k}}{h_k}\right)\right]. \tag{16.10}$$

To evaluate whether the above independent assumption fits the data, we borrow the information complexity (ICOMP) criterion proposed by Bozdogan [3]. The ICOMP criterion is chosen since it has the following advantages. Firstly, it allows the measurement of dependency between the random variables. Secondly, it establishes and provides a trade-off between the fit and the interaction between the parameter estimates and the residuals of a model via the measure of complexity of their respective covariances. The redundancy measure based on the ICOMP is given by:

$$R(\mathscr{B}_m) = -2\log L(\mathbf{s}_1,\ldots,\mathbf{s}_N \mid h_k) + 2C_{1F}\big(\hat{\Sigma}\big), \tag{16.11}$$

where $\hat{\Sigma}$ denotes the estimated covariance matrix. The first term in the above equation evaluates the fitting error whereas the second term considers the complexity of the estimated covariance matrix, which indicates the correlation among variables. The fitting error term is given by:

$$-2\log L(\mathbf{s}_1,\ldots,\mathbf{s}_N \mid h_k) = \sum_{i=1}^{N}\log \hat{p}_{-i}(\mathbf{s}_i), \tag{16.12}$$

where $\hat{p}_{-i}(\mathbf{x})$ is the leave-one-out estimator:

$$\hat{p}_{-i}(\mathbf{x}) = \frac{1}{N-1}\sum_{j=1, j\neq i}^{N}\left[\prod_{k=1}^{N_k}\frac{1}{h_k}K\left(\frac{x_k - S_{jj}^{k}}{h_k}\right)\right]. \tag{16.13}$$

The $C_{1F}(\hat{\Sigma})$ is the second order equivalent measure of the complexity of the C_1 measure:

$$C_{1F}\big(\hat{\Sigma}\big) = \frac{s}{4}\frac{C_1(\hat{\Sigma})}{(\mathrm{tr}(\hat{\Sigma})/s)^2}, \tag{16.14}$$

where the information complexity C_1 is defined as:

$$C_1\big(\hat{\Sigma}\big) = \frac{s}{2}\log\left[\frac{\mathrm{tr}(\hat{\Sigma})}{s}\right] - \frac{1}{2}\log\big|\hat{\Sigma}\big| \tag{16.15}$$

and $s = \mathrm{rank}(\hat{\Sigma})$. The estimated covariance matrix is computed by:

$$\hat{\Sigma} = \hat{F}^{-1}\hat{R}\hat{F}^{-1}, \tag{16.16}$$

where $\hat{F}^{-1}$ is the inverse Fisher information estimation and $\hat{R}$ is the estimated outer-product form of the Fisher information.

16.5 Experimental Results

In order to demonstrate the effectiveness of the band selection algorithm, six sets of experiments are designed, including simulated and real data. The experimental results demonstrate that face recognition rate can be substantially improved over that of the conventional broad-band images for both indoor and outdoor environments. In addition, a simplified multispectral face imaging system can be engineered with reduced acquisition and processing time.

16.5.1 Simulated Data

In this section, the performance of the proposed band selection algorithms is studied via simulated data. Simulated data sets are deliberately included for experimentation with controlled parameters, where one can quantitatively compare the results with the known groundtruth values. As mentioned previously, the input parameters to the proposed algorithm are sets of genuine $\mathscr{G}_k$ and imposter $\mathscr{I}_k$ similarity scores. To achieve a close resemblance to the real data, similarity scores are computed by the Identix's FaceIt [19] recognition engine based on the IRIS-M^3 face database and their distributions are studied, which leads to the following main observations. (1) The distributions of the similarity scores of the imposter sets collected at different spectral locations share a similar distribution, which can be modeled as a Gaussian with zero mean and unit variance. (2) The distributions of the similarity scores of genuine sets resemble a Gaussian with comparable variances but different means. (3) The correlation between two sub-bands decreases with respect to the increase in the spectral distance between the sub-bands.

Based on these observations, the simulated data is designed as follows. The center wavelength of simulated sub-spectral bands are distributed uniformly in a spectral range of 480 nm to 720 nm with a 10 nm increment. The similarity scores of the imposter sets for all sub-bands are drawn from a Gaussian with zero mean and unit variance. In a Matlab implementation, this is done by calling the function *randn()* with default settings. Considering the correlation of the genuine similarity scores among sub-bands, the scores are drawn from a multivariate Gaussian. Its mean and covariance values determine the system's behavior and are the controlled parameters in the simulated experiments. The specific mean and covariance values used in the experiments will be given in the discussions regarding the experimental results. Once the mean and covariance values are designed, 500 samples are drawn from the multivariate Gaussian for each set. In a Matlab implementation, this is done by calling the function *mvnrnd()* with given mean and covariance.

The mean and covariance values of the simulated data for the first experiment are shown in Fig. 16.10(a). The data is designed such that the optimal number of bands is three and they are 720 nm, 630 nm, and 550 nm, depicted as the local peaks in Fig. 16.10(a). Multiple peaks are deliberately introduced in the design of this experiment to test the ability of the proposed algorithm in picking up the correct

Fig. 16.10 **a** The mean and covariance of the simulated data. The correlation values are shown for bands 480 nm, 580 nm, and 680 nm. The correlation with a given band decreases linearly as the wavelength of the sub-band moves away from the center wavelength of the given band. **b** Normalized distance measure values for 25 bands with three local peaks. **c** Redundancy measures for different number of bands with three bands having the minimal value

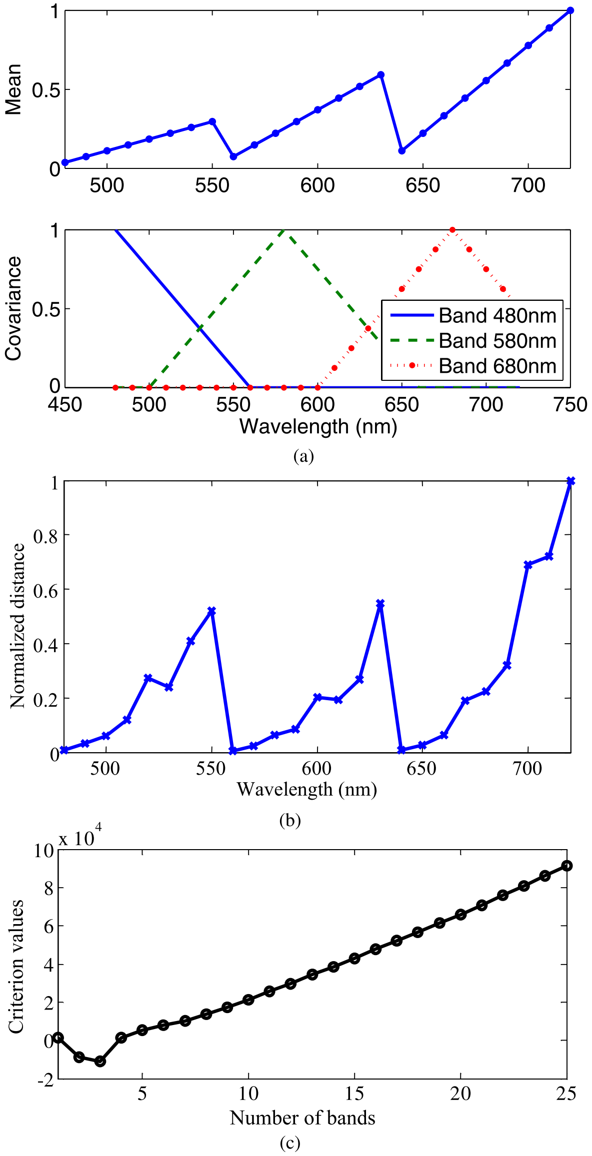

number of optimal bands. In addition, the correlation of these data sets is designed such that these peaks are uncorrelated, resulting in an optimal number of sub-bands of three. The computed distance values are shown in Fig. 16.10(b), where we observe three peaks, which agrees with the actual optimal bands. This verifies the ability of the proposed algorithm in correctly locating the potential optimal bands. Figure 16.10(c) shows the redundancy measure with a minimum value at three, suggesting that the three peaks are sufficient to represent the remaining sub-bands. This agrees with the structure of the simulated data and verifies the ability of the proposed algorithm in not only locating the optimal bands but also selecting the correct number of bands to form a sufficient and necessary subset.

Although, by design, bands 710 nm and 700 nm produce higher distance measures, they are highly correlated with band 720 nm. Therefore, they are excluded from the optimal subset selected via the newly proposed redundancy measure. In comparison, the band ranking algorithm described in [8, 9] selects 700 nm, 710 nm, and 720 nm if $N_{\text{opt}} = 3$ is given. The more informative bands 550 nm and 630 nm are not selected. The proposed algorithm selects the optimal bands and decides the number of bands with consideration of both distance values and the correlation among the bands.

In the second experiment, the correlation among spectral bands is increased, as shown in Fig. 16.11(a). With the increased correlation, we expect to see a decreased number of selected sub-bands. Figure 16.11(b) shows the distance measure values from these 25 bands, and the corresponding redundancy measure is given in Fig. 16.11(c). Disregarding the four peaks illustrated in Fig. 16.11(b), only two sub-bands 710 nm and 530 nm are selected primarily because of the increased correlation among sub-bands.

The experimental results based on simulated data clearly illustrate the power of the proposed selection process. Instead of simply ranking multiple spectral bands according to their probabilistic distance measure, the proposed algorithm can adaptively and automatically select the most representative and informative bands according to the recognition capacity of the bands and their correlations.

16.5.2 Real Data

That selecting the optimal spectral bands from a series of multispectral images under given illuminations improves face recognition performance can be shown in the following experiments with real data. Four experiments are designed to investigate the recognition performances of fused images from the selected band/bands in comparison with conventional broad-band images. In real world situations, face images are frequently acquired under different lighting conditions and compared with the database images. It is reasonable and important to study the situation that the illuminations for gallery and probe images are different. The IRIS-M^3 face database is used because it contains gallery and probe images collected under various illuminations. According to the available lighting sources in the IRIS-M^3 face database, the following four sets of experiments were conducted with the gallery and probe sets collected from different illuminations. Table 16.2 lists the experimental conditions.

In these experiments, similarity scores are obtained via Identix's FaceIt [19], a well-known recognition engine. Jeffrey divergence values are normalized between 0 and 1 for clear illustration. If more than two bands are selected, for example, Haar wavelet-based pixel-level fusion [15], can be applied for the fusion of images from the selected sub-bands. Given the registered narrow-band images from the selected

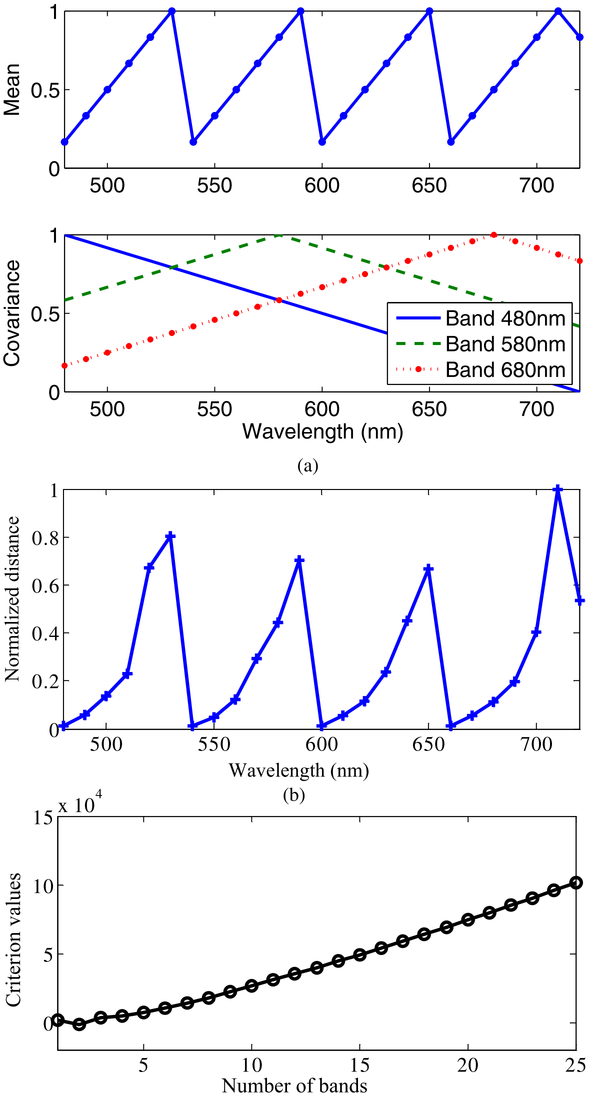

Fig. 16.11 **a** The mean and covariance of the simulated data. The correlation values are shown for bands 480 nm, 580 nm, and 680 nm. Spectral bands are highly correlated. **b** Normalized distance measure values for 25 bands with four local peaks. **c** Redundancy measures for different number of bands with two bands having the minimal value

(a)

(b)

(c)

spectral range, two-dimensional discrete wavelet decomposition is performed on each image to obtain the wavelet approximation coefficients and detail coefficients. The coefficients in inverse wavelet transform for fused image are obtained by choosing the maximum among each type of coefficients. The two-dimensional discrete wavelet inverse transform is then performed to construct the fused image.

In addition to the rank-one recognition rate, a numerical measure is used to evaluate the recognition performance. To enable quantitative comparison of the overall performances at different ranks, a mapping operation projecting the multi-index

Table 16.2 Experimental conditions including the description of the gallery lighting, probe lighting, spectral range, and the number of sub-bands

	Gallery	Probe			
		Illumination	Spectral range	Increment	Num. of bands
Experiment 1	Fluorescent	Halogen	480 nm–720 nm	10 nm	25
Experiment 2	Day light	Halogen	480 nm–720 nm	10 nm	25
Experiment 3	Fluorescent	Day light	480 nm–720 nm	20 nm	13
Experiment 4	Halogen	Day light	480 nm–720 nm	20 nm	13

CMC curve to a single number, CMCM, is defined as:

$$\mathrm{CMCM} = \sum_{r=1}^{N} \frac{C_r}{rN}, \tag{16.17}$$

where r represents the rank number, and C_r denotes the number of probe images that can be correctly identified at and below rank r. Recall that N denotes the total number of subjects in the gallery. The factor $1/r$ can be viewed as a weight, which decreases monotonously as r increases. As a result, the rank-one recognition rate is dominant and contributes the most to the value of CMCM. A better face recognition performance is indicated by a higher CMCM value, which varies between 0 and 1.

In Fig. 16.12, the normalized probability distance is given whereas the redundancy measure via ICOMP calculation of each possible number of selected bands is given in Fig. 16.13. For all experiments, the proposed algorithm selected one band. The selected bands are 610 nm, 610 nm, 720 nm, and 720 nm for the four experiments, respectively. The reason why only one band is selected lies in the fact that the correlation among all the bands is relatively high. To validate the selection results, face recognition performances including the rank-one recognition rate and CMCM values of the selected bands are tested and given in Table 16.3 in comparison with those of the conventional broad-band images. The images from a single selected band outperform the conventional broad-band monochromatic images. Taking Experiment 1 as an example, the recognition performance is improved by relatively $9.7\%((97.14 - 88.56)/88.56 \times 100\% = 9.7\%)$ of rank-one rate and by $4.5\%((98.57 - 94.28)/94.28 \times 100\% = 4.5\%)$ of the CMCM value.

Table 16.3 also lists the performance comparison between the proposed algorithm and the reference algorithm developed in [8, 9]. For Experiment 2 and 4, the images from a single band selected by the proposed algorithm outperform the fused images from three selected bands via the reference algorithm. For the other two experiments (Experiment 1 and 3), their performances are comparable. Note that image fusion helps to reduce image noise, which may also lead to improved recognition performance. This explains the observed comparable performance in Experiments 1 and 3. Therefore, we could conclude that the proposed algorithm is capable of identifying the most concise subset with the most informative spectral bands.

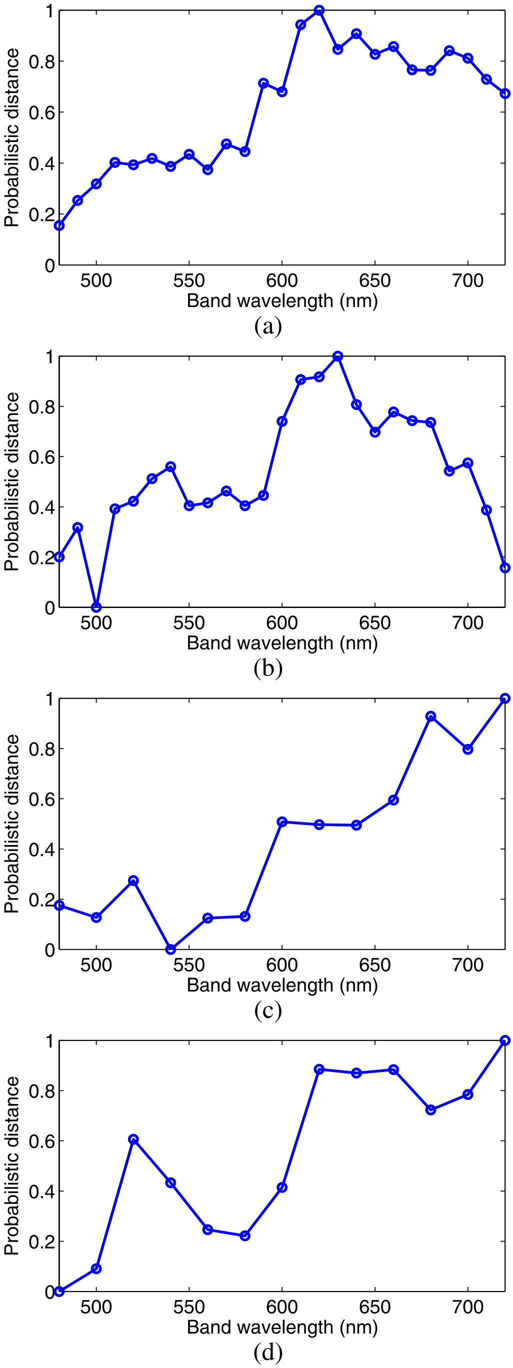

Fig. 16.12 Normalized distance measures for multiple spectral bands: **a** Experiment 1, **b** Experiment 2, **c** Experiment 3, and **d** Experiment 4

Fig. 16.13 Redundancy measure for different number of selected sub-bands: **a** Experiment 1, **b** Experiment 2, **c** Experiment 3, and **d** Experiment 4

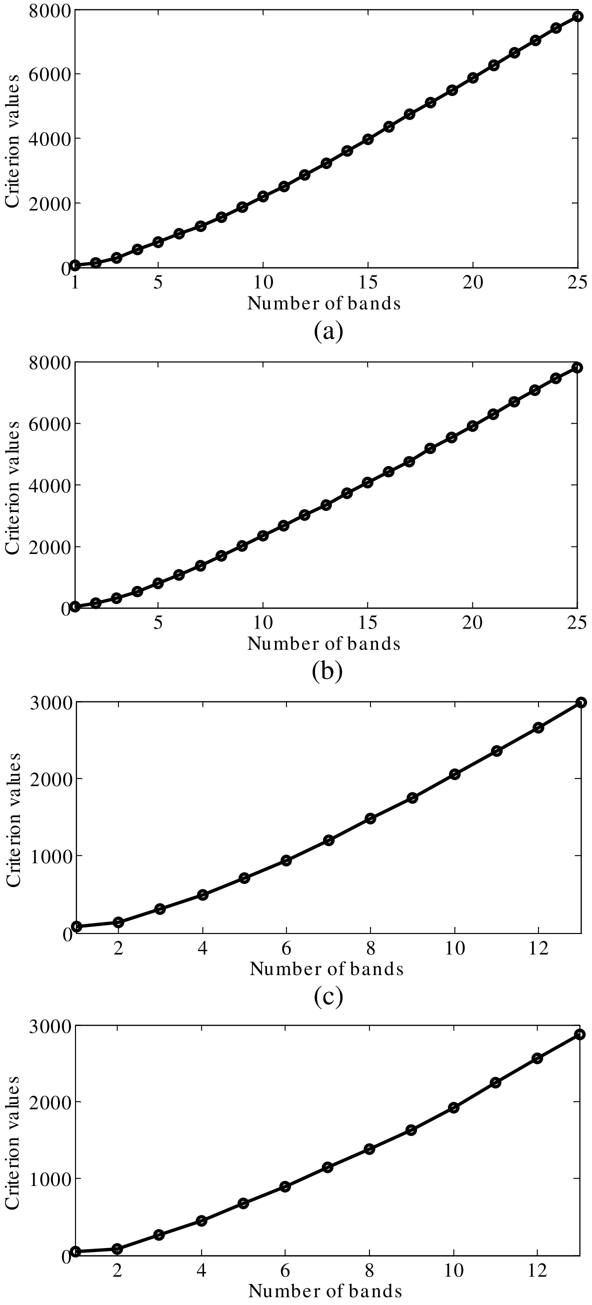

(a)

(b)

(c)

(d)

Table 16.3 Rank-one and CMCM recognition rates of the monochromatic conventional broad-band image, the fused narrow-band images via the reference algorithm [8, 9], and the selected narrow-band images via the proposed algorithm

	The proposed algorithm	Broad-band	Improvement	Reference [8, 9]	Improvement
Experiment 1					
Rank-one	97.14	88.56	9.7	97.14	0.0
CMCM	98.57	94.28	4.5	98.57	0.0
Experiment 2					
Rank-one	65.17	57.15	15.0	62.86	3.7
CMCM	74.06	70.20	5.5	72.11	2.7
Experiment 3					
Rank-one	97.14	94.28	3.0	97.14	0.0
CMCM	97.57	95.36	3.4	98.57	−1.0
Experiment 4					
Rank-one	54.29	48.57	11.8	48.57	11.8
CMCM	64.79	57.28	13.1	60.84	6.5

16.6 Conclusions

In this chapter, the fundamentals of multispectral imaging and its applications to face recognition were introduced. Variation in illumination dramatically degrades face recognition performance. Narrow-band sub-spectral images were used instead of conventional broad-band images to improve recognition performance. A spectral band selection algorithm was developed to choose the optimal band images under given illumination conditions. From the experiments, the spectral bands of 610 nm and 720 nm are the optimal choice for probes under indoor halogen light and varying daylight, respectively. The selected optimal spectral bands are consistent with those specified by physics analysis with known system configuration and illumination characteristics and result in a 3%–15% improvement in face recognition rate in comparison with that of conventional broad-band images. In addition, the optimal set ensures a minimum amount of acquisition and processing time for fast face recognition by selecting the most informative and independent sub-bands.

Acknowledgements This work was supported in part by the DOE University Research Program in Robotics under grant DOE-DEFG02-86NE37968 and NSF-CITeR grant 01-598B-UT.

References

1. Bajcsy, P., Groves, P.: Methodology for hyperspectral band selection. Photogramm. Eng. Remote Sens. **70**, 793–802 (2004)
2. Bassett, E.M., Shen, S.S.: Information theory-based band selection for multispectral systems. In: SPIE, vol. 3118, pp. 28–35 (1997)

3. Bozdogan, H.: Akaike's information criterion and recent developments in information complexity. J. Math. Psychol. **44**, 62–91 (2000)
4. Bruce, L., Koger, C., Li, J.: Dimensionality reduction of hyperspectral data using discrete wavelet transform extraction. IEEE Trans. Geosci. Remote Sens. **40**(10), 2331–2338 (2002)
5. Brusco, M.J.: An enhanced branch-and-bound algorithm for a partitioning problem. Br. J. Math. Stat. Psychol. **56**, 83–92 (2003)
6. Bruzzone, L., Roli, F., Serpico, S.B.: An extension of the Jeffreys–Matusita distance to multiclass cases for feature selection. IEEE Trans. Geosci. Remote Sens. **33**(6), 1318–1321 (1995)
7. Chang, C.I., Du, Q., Sun, T.S., Althouse, M.L.G.: A joint band prioritization and band decorrelation approach to band selection for hyperspectral image classification. IEEE Trans. Geosci. Remote Sens. **37**(6), 2631–2641 (1999)
8. Chang, H., Yao, Y., Koschan, A., Abidi, B., Abidi, M.: Spectral range selection for face recognition under various illuminations. In: IEEE Int'l Conf. on Image Processing, San Diego, CA, October 2008
9. Chang, H., Yao, Y., Koschan, A., Abidi, B., Abidi, M.: Improving face recognition via narrowband spectral range selection using Jeffrey divergence. IEEE Trans. Inf. Forensics Secur. **4**(1), 111–122 (2009)
10. Chang, H., Koschan, A., Abidi, B., Abidi, M.: Fusing continuous spectral images for face recognition under indoor and outdoor illuminants. Mach. Vis. Appl. **21**, 201–215 (2010)
11. Du, H., Qi, H., Wang, X., Ramanath, R., Snyder, W.E.: Band selection using independent component analysis for hyperspectral image processing. In: Applied Imagery Pattern Recognition Workshop, pp. 93–98 (2003)
12. El-ghazawi, T., Kaewpijit, S., Le Moigne, J.: Parallel and adaptive reduction of hyperspectral data to intrinsic dimensionality. In: IEEE Int'l Conf. on Cluster Computing (2001)
13. Finlayson, G.D., Morovic, P.M., Hordley, S.D.: Using the spectracube for multispectral imaging. In: 2nd Conference on Color in Imaging, Vision and Graphics, pp. 268–274 (2004)
14. Gat, N.: Imaging spectroscopy using tunable filters: a review. In: SPIE, vol. 4056, pp. 50–64 (2000)
15. Gonzalez, R., Woods, R.: Digital Image Processing. Prentice Hall, New York (2004)
16. Gottlieb, M.S.: Acousto-optic tunable filters. In: Design and Fabrication of Acousto-Optic Devices, pp. 197–284. Marcel Dekker, New York (1994)
17. Hardeberg, J.Y., Schmitt, F., Brettel, H.: Multispectral image capture using a liquid crystal tunable filters. Opt. Eng. **41**(10), 2532–2548 (2002)
18. Healey, G., Slater, D.: Invariant recognition in hyperspectral images. In: IEEE Conf. on Computer Vision and Pattern Recognition, pp. 438–443, Ft. Collins, CO, June 1999
19. http://www.identix.com/pages/101-faceit-sdk
20. Imai, F.H., Berns, R.S.: High-resolution multispectral image archives: a hybrid approach. In: IS&T SID Sixth Color Imaging Conf., pp. 185–189 (1998)
21. Imai, F.H., Rosen, M.R., Berns, R.S.: Multi-spectral imaging of a van Gogh's self-portrait at the National Gallery of Art, Washington, D.C. In: IS&T PICS, pp. 185–189 (2001)
22. Jeffreys, H.: An invariant form for the prior probability in estimation problems. Proc. R. Soc. **186**, 453–461 (1946)
23. Jiang, L., Mann, B., Mathur, A.: Wavelet transform for dimensionality reduction in hyperspectral linear unmixing. In: IEEE Int'l Geoscience and Remote Sensing Symposium, vol. 6, pp. 3513–3515 (2002)
24. Jimenez, L.O., Landgrebe, D.A.: Supervised classification in high dimensional space: geometrical statistical and asymptotical properties of multivariate data. IEEE Trans. Syst. Man Cybern. **28**(1), 39–54 (1998)
25. Kohavi, R., John, G.H.: Wrappers for feature subset selection. Artif. Intell. **97**, 273–324 (1997)
26. Koller, D., Sahami, M.: Towards optimal feature selection. In: Int'l Conf. on Machine Learning, pp. 284–292, Bari, Italy, July 1996
27. Korycinski, D., Crawford, M.M., Barnes, J.W.: Adaptive feature selection for hyperspectral data analysis using a binary hierarchical classifier and tabu search. In: Int'l Geoscience and Remote Sensing Symposium, pp. 297–299 (2003)

28. Kudo, M., Sklansky, J.: Comparison of algorithms that select features for pattern classifiers. Pattern Recognit. **33**(1), 25–41 (2000)
29. Kuman, S., Ghosh, J., Crawford, M.M.: Best basis feature extraction algorithms for classification of hyperspectral data. IEEE Trans. Geosci. Remote Sens. **39**(7), 1368–1379 (2001)
30. Lennon, M., Mercier, G., Mouchot, M., Hubert-Moy, L.: Independent component analysis as a tool for the dimensionality reduction and the representation of hyperspectral image. In: IEEE Int'l Geoscience and Remote Sensing Symposium, vol. 6, pp. 2893–2895 (2001)
31. Liu, C., Wechsler, H.: A unified Bayesian framework for face recognition. In: IEEE Int'l Conf. on Image Processing, pp. 151–155, Chicago, IL, October 1998
32. Mugdadi, A.R., Munthali, E.: Relative efficiency in kernel estimation of the distribution function. J. Stat. Res. **37**(2), 203–218 (2003)
33. Ohta, N., Takahashi, K., Urabe, H., Miyagawa, T.: Image simulation by use of a laser color printer. O plus E **22**, 57–64 (1981)
34. Pan, Z., Healey, G., Prasad, M., Tromber, B.: Face recognition in hyperspectral images. IEEE Trans. Pattern Anal. Mach. Intell. **25**(12), 1552–1560 (2003)
35. Pan, Z., Healey, G., Prasad, M., Tromberg, B.: Hyperspectral face recognition under variable outdoor illumination. In: SPIE, vol. 5425, pp. 520–529 (2004)
36. Parkkinen, J., Oja, E., Jaaskelainen, T.: Color analysis by learning subspaces and optical processing. In: Int'l Conf. on Neural Networks (1988)
37. Parzen, E.: On estimation of a probability density function and model. Ann. Math. Stat. **33**(3), 1065–1076 (1962)
38. Peng, H., Long, F., Ding, C.: Feature selection based on mutual information criteria of max-dependency, max-relevance, and min-redundancy. IEEE Trans. Pattern Anal. Mach. Intell. **27**(8), 1226–1238 (2005)
39. Poger, S., Angelopoulou, E.: Selecting components for building multispectral sensors. In: IEEE CVPR Technical Sketches (2001)
40. Rosen, M., Jiang, X.: Lippmann2000: a spectral image database under construction. In: Int'l Symposium on Multispectral Imaging and Color Reproduction for Digital Archives, pp. 117–122 (1999)
41. Roweis, S.T., Saul, L.K.: Nonlinear dimensionality reduction by locally linear embedding. Science **290**, 2323–2326 (2000)
42. Slater, D., Healey, G.: Physics-based model acquisition and identification in airborne spectral images. In: Int'l Conf. on Computer Vision, pp. 257–262, Vancouver, British Columbia, Canada, July 2001
43. Sotoca, J.M., Pla, F., Klaren, A.C.: Unsupervised band selection for multispectral images using information theory. In: Int'l Conf. on Pattern Recognition, vol. 3, pp. 510–513, Cambridge, UK, August 2004
44. Tenenbaum, J.B., Silva, V., Langford, J.C.: A global framework for nonlinear dimensionality reduction. Science **290**, 2319–2323 (2000)
45. Tominaga, S.: A multi-channel vision system for estimating surface and illuminant functions. J. Opt. Soc. Am. A **13**, 2163–2173 (1996)
46. Vidal-Naquet, M., Ullman, S.: Object recognition with informative features and linear classification. In: IEEE Int'l Conf. on Computer Vision, pp. 281–288, Nice, France, October 2003
47. Wang, H., Angelopoulou, E.: Sensor band selection for multispectral imaging via average normalized information. J. Real-Time Image Process. **1**(2), 109–121 (2006)
48. Wasserman, L.: All of Statistics: A Concise Course in Statistical Inference. Springer Texts in Statistics (2005)